Deep-sea benthic structures and substrate types influence the distribution of functional groups in the Wallaby-Zenith Fracture Zone (East Indian Ocean)

Yakufu Niyazi*[1] Todd Bond[1], Jessica L. Kolbusz[1], Paige J. Maroni[1], Heather A. Stewart[2], Alan J. Jamieson[1]

[1]Minderoo-UWA Deep-Sea Research Centre, School of Biological Sciences and UWA Oceans Institute, The University of Western Australia, Perth, Western Australia 6009, Australia

[2]British Geological Survey, Lyell Centre, Research Avenue South, Edinburgh, EH14 4AP, UK

*Corresponding author: yakup.niyazi@uwa.edu.au

Abstract

Three-dimensional deep-sea structures enhance substrate complexity and can shape numerous ecological hotspots that play critical roles in the diversity and distribution of benthic faunal assemblages. The characteristics of these features are not fully understood due to the logistical challenges of exploring at great depths and remote locations. One such deep-sea feature, the Wallaby-Zenith Fracture Zone (WZFZ) located in the East Indian Ocean, was mapped using a full-ocean depth multibeam echosounder system. Additionally, twelve baited landers and five crewed submersible dives were conducted in water depths of between 4709 and 6591 m. We use seafloor bathymetry, bathymetric derivatives and video footage from the submersible dives to characterise the benthic structures, substrate types, habitat diversity, and the distribution of associated functional groups of megafauna for the WZFZ. The Benthic Terrain Modeler toolbox was used as an initial semi-automated step to generate benthic structural classes, which were then refined through the inclusion of bottom salinity and temperature data collected by the scientific landers and integrated with the observations of seafloor substrate from the submersible video footage. This resulted in identification of nine benthic habitat classes characterised by unique seafloor morphological structure and substrate texture. A polymetallic nodule field, a possible extension of the previously reported Cape Leeuwen nodule field, was also observed along submersible transects conducted on the slopes of the WZFZ. The distribution and diversity of the functional megafauna groups observed are influenced by the deep-sea benthic habitats, defined by seafloor structures and substrate heterogeneity, especially the presence of hard substrates such as outcropping bedrock and polymetallic nodules within the WZFZ.

Keywords: Deep-sea habitat, Fauna assemblage, Polymetallic nodules, Wallaby-Zenith Fracture Zone, Indian Ocean.

1. Introduction

The world's oceans cover approximately 71% of Earth's surface area, and the abyssal and hadal zones (deeper than 3000 m) represent the largest environment on the planet, accounting for 75.3% of the entire ocean (Weatherall et al., 2015; Stewart and Jamieson, 2019). Much of this vast and remote marine realm remains relatively understudied compared to terrestrial or shallower water environments. With growing anthropogenic pressure on the deep sea, multidisciplinary studies provide a greater understanding of habitats and their associated biological communities and can offer more robust insights when considering the necessity of sustainable spatial management (Harris and Baker, 2011; Davies et al., 2015). Deep-sea structures, substrates and benthic habitats are not only fundamental to understanding fully the oceans' ecosystems and their resilience, but are also at the core of recognising its spatial variabilities and utilising the marine environment sustainably.

The Indian Ocean is the world's third-largest ocean, accounting for 19.8% of the global ocean volume, and is arguably the least understood of the five oceans from a biological exploration perspective (Stefanoudis et al., 2020; Jamieson et al., 2022). Seamounts, ridges, plateaus, submarine fans, coral atolls, fracture zones, and hydrothermal vents are abundant in the Indian Ocean and likely play important roles in maintaining biodiversity (Wafar et al., 2011; Wolff et al., 2011; Harris et al., 2014;

Weston et al., 2020, 2021; Jamieson et al., 2022; Swanborn et al., 2022) (Figure 1). The Indian Ocean also hosts many fracture zones formed through the extension of transform faults between oceanic tectonic plates (Menard and Atwater, 1969). These fracture zones are long and narrow features comprising complex topography that disrupt the surrounding morphology, resulting from the action of offset mid-ocean ridge axis segments (Fox et al., 1976; Tucholke and Schouten, 1988; IHO, 2008; Harff et al., 2016; Nansen et al., 2023). They can extend for hundreds or thousands of kilometres in length (Bird, 2001; Harff et al., 2016), and frequently exceed 5000 m water depth (Heezen et al., 1964) with several known to exceed 6000 m (Mercier and Morin, 1997; Stewart and Jamieson, 2018). The most conspicuous fracture zone in the East Indian Ocean is the Diamantina Fracture Zone (DFZ; Mammerickx and Sandwell, 1986). North of the DFZ a network of smaller fracture zones, toughs, and escarpments are present, bounded by the Wharton Basin to the north at 20° S (Jacob et al., 2014; Picard et al., 2018) (Figure 1a).

A lesser known, and comparatively smaller fracture zone than the DFZ, is the Wallaby-Zenith Fracture Zone (WZFZ) that extends from the western Australia continental margin, trending northwest around 2000 km, and has a width of ~200 km (Gibbons et al., 2012; Olierook et al., 2015). The WZFZ is a structurally complex area of rugged topography composed of numerous plains, troughs, and ridges (Gibbons et al., 2012; Harris et al., 2014; Bond et al., 2023). This heterogeneous seafloor structure combined with a diverse range of environmental features may have facilitated a variety of habitat types that have the potential to support a distinctive assemblage of benthic organisms (Bowden et al., 2015; Zeppilli et al., 2016; Bond et al., 2023). Despite its conspicuous regional presence on bathymetric charts, the WZFZ has received little scientific examination of its morphology, habitat, and ecology; limited only to amphipod studies (Weston et al., 2020, 2021).

Further, the Indian Ocean is known to host polymetallic nodule fields confined mainly to the Central Indian Ocean Basin (Vineesh et al., 2009; Hein et al., 2013). Polymetallic nodules, also known as ferromanganese nodules or manganese nodules, are often rich in a variety of metals such as nickel, cobalt, copper, titanium, and rare earth elements (Hein and Koschinsky, 2014; Kuhn et al., 2017; Hein et al., 2020). In addition to their economic value, the hard substratum provided by the nodules, combined with the surrounding soft sediment, promotes habitat complexity, and supports the occurrence of some of the most biologically diverse seafloor assemblages in the abyss (Amon et al., 2016; Gooday et al., 2017; Uhlenkott et al., 2023). A large manganese nodule field - the Cape Leeuwin manganese nodule field, was discovered on the northern flank of the Southeast Indian Ridge and DFZ (Figure 1a) via bottom dredging and free fall grab sampling (Kennett and Watkins, 1976, 1975; Frakes, 1982). Yet, the northern boundary of this nodule field and associated megafauna remain unknown.

The DSSV (Deep Submersible Support Vessel) *Pressure Drop* (renamed RV *Dagon*) undertook expedition “Indomitable” in 2021 to the poorly explored WZFZ to (1) acquire high-resolution multibeam echosounder (MBES) bathymetric data; (2) characterize the major benthic structures and oceanographic bottom conditions; (3) examine the substratum types and the presence or absence of polymetallic nodules; and (4) assess controls on the distribution of benthic functional groups. Bathymetric data was collected by using a full ocean depth MBES system, and essential deep-sea benthic structures were derived from this high-resolution seafloor map. The vessel was also equipped with three free-fall scientific landers and a submersible (Figures 1 and 2). Oceanographic bottom conditions such as temperature and salinity were collected by 12 lander deployments to provide environmental characterization of the structural classes. The substrate types and benthic megafauna distribution were analysed based on the video observations along the submersible dive transects. Finally, these datasets were integrated to analyse the benthic structure and substrates influencing the distribution of functional groups in the study area (Figure 2).

2. Materials and Methods

2.1. Study Area

The study area encompasses the northwestern portion of the WZFZ (22° S / 122° E) where the Lost Dutchman Ridge meets the East Indiaman Ridge, to the southwest of the Zenith Plateau of the East Indian Ocean (Figure 1b). The WZFZ formed as a transform fault between 130-124 Ma with the opening of the Indian Ocean during the breakup of Greater India and Australia along the northwest-southeast trending fracture zone (Veevers and Cotterill, 1978; White et al., 2013; Olierrok et al., 2015). Regional bathymetric, magnetic, and gravity data indicate that the fracture zone extends from the west Australian continental margin around 2000 km to the northwest and has a width of ~200 km, significantly wider than other fracture zones and may indicate an oblique component of movement during breakup in the region (Daniell et al., 2010; Olierook et al., 2015) (Figure 1b). The fracture zone bounds the northern limit of the Perth Abyssal Plain and is composed of several offset ridges such as the Lost Dutchman Ridge that is oriented at acute angles to its southern edge (Nelson et al., 2009). During the SO258 expedition in 2017, the RV *SONNE* mapped part of the WZFZ and suggested the fracture zone has a maximum depth of 6625 m (Werner et al., 2017; Weston et al., 2021). That expedition also observed a potential polymetallic nodule field comprising spherical nodules and fragments of crusts within soft sediment matrix.

The WZFZ lies within the Indian Ocean South Subtropical Gyre biogeochemical province with a low primary production rate of 71 g C m^{-2} $year^{-1}$ (Longhurst et al., 1995). The upper ocean properties are driven by the South Equatorial Current, which carries fresher Pacific waters across the width of the Indian Ocean. In contrast to the Pacific and Atlantic oceans, deep bottom waters spread northward along the western and eastern sides of the Indian Ocean. The complex seafloor topography allows for three bottom-water pathways, one of which reaches the WZFZ, originating in the Ross Sea, Antarctica. This Antarctic Bottom Water (AABW) is higher in salinity and temperature than other Antarctic-derived bottom waters (Gordon and Tchernia, 1978; Talley, 2011). The AABW mixes with dense water from the Antarctic Circumpolar Current, entering the Australian-Antarctic Basin and eventually reaching the eastern Indian Ocean through the South Australia Basin near 33° S / 105° E (Mantyla and Reid, 1995).

2.2. Data collection

The datasets used in this study were collected during the expedition “Indomitable” on the DSSV *Pressure Drop* in May 2021. The vessel was equipped with a full ocean depth MBES, autonomous free-fall scientific landers and a crewed submersible vehicle.

2.2.1. Multibeam echosounder data

The DSSV *Pressure Drop* is equipped with a hull-mounted, full ocean depth EM124 MBES (Kongsberg, Norway), see Bongiovanni et al. (2022) for detailed acquisition parameters of the EM124 on board this vessel. Processing of MBES data was accomplished using QPS Qimera (v.2.5) software. Data were filtered using both manual editing and automatic filtering functions. A Digital Bathymetric Model (DBM) with a 100 m cell grid size was generated in order that at least 99.6% of the cells had a minimum of 5 soundings to ensure production of a robust, high-resolution surface map (Supplementary Figure S1). Small data gaps within the DBM were filled 3×3 matrix sizes to create a smooth and continuous bathymetric surface. The final DBM was analysed in ArcGIS (v.10.8) software.

2.2.2. Submersible and scientific landers

Five crewed dives were conducted during the expedition using DSV *Limiting Factor* (LF) (Figure 1c and d, Table 1). The LF (built by Triton Submarines for Caladan Oceanic LLC), a full ocean depth-rated (up to 11 km) submersible has three fixed-position high-definition video cameras (IP Multi SeaCam 3105, DeepSea Power & Light, San Diego, US) and ten 15,500 lumen LED lights (LED-1153-A3-SUS, Teledyne Bowtech, Aberdeen, UK) for illumination (Jamieson et al., 2019). Each submersible dive was performed at a relatively constant altitude off the seafloor, with a mean speed of 20 m min^{-1} and 10 m min^{-1} for the flat and vertical terrain dives respectively (Jamieson et al., 2022). During the transects undertaken on relatively flat regions the horizontal field of view of the camera is around 3 m. Water depth, heading (in degrees) and horizontal position was calculated based on the relative location of the submersible to the supporting landers, and was recorded every half hour during each dive.

Three identical landers (known as *Skaff, Flere* and *Closp*) were used in unison to support LF's diving operations and collected data from a total of 12 deployments (Figure 1c and d, Table 2) (e.g., Jamieson et al., 2021). The autonomous landers were deployed from the ship and descended to the seafloor, and each of them was equipped with a conductivity (for salinity), temperature, and depth (CTD) probe (SBE 49 FastCAT; SeaBird Electronics, Bellevue, US). The CTDs sample at 10-second intervals and measure conductivity, temperature, and pressure at ± 0.0003 S m^{-1}, ±0.002 ^{o}C and ±0.1% of the full-scale range, respectively (Sea-Bird Scientific, 2020).

2.3. Data analysis

2.3.1. Bathymetric derivatives and seafloor structural classification

A "top down" hierarchical classification scheme was used to define the seafloor structure of the study area (Greene et al.,1999 and 2007). In the "top down" methodology, the acoustic datasets are first classified into areas of similar pattern (seabed structures in this study) and then characterized using a combination of underwater video and/or environmental data. To classify the seabed structures, a set of bathymetric derivatives were calculated using the Benthic Terrain Model (BTM, v.3.0) tool, an extension to ArcGIS (v.10.8) software (Walbridge et al., 2018). Derivatives such as slope, aspect, terrain ruggedness (sometimes referred to as rugosity), and bathymetric position index (BPI) were calculated using the DBM as input (Figure 3). The BPI is a pixel-based surface measurement that compares the depth of each cell to the mean depth of the user-defined number of neighbourhood cells in an annulus (Lundblad et al., 2006; Walbridge et al., 2018). Positive BPI values indicate bathymetric highs, such as ridges, while negative BPI values indicate bathymetric lows such as troughs. In this study, the DBM, slope, BPI, and a table containing definitions and thresholds unique to each structural class were used as input for the seafloor classification process of the BTM (Figure 3). The BTM uses the combination of these derived terrain attributes to classify the seafloor into structural classes.

As spatial data tend to be scale dependent, BPI differentiates benthic features at both fine and broad scales. For instance, a broad slope can appear as a ridge using a fine scale BPI window, while the same area may more resemble a flat plain at broader BPI scale. Combining BPI at both fine and broad scales allows for the distinction of a variety of nested features and removes interpreter bias. To select the best scale factor, BPI was calculated using different inner and outer radii (5×10, 5×20, 5×30, 10×20, 10×30, 10×40, 20×30, 20×40, 20×50, 30×40, 30×50) (Supplementary Figure S2). We discovered that fine scale detail was lost when the inner and outer radius values exceeded 10×20, with only broad trends identified at the 20×50 scale and with larger radius the seabed seem to have been 'flattened' (Supplementary Figure S2). Therefore, inner and outer radii of 10×20 and 20×50 were selected for the fine and broad BPI scale factors, respectively. These scale factors were used to generate BPI maps for the study area and were standardised to avoid the influence of spatial autocorrelation (Weiss, 2001; Erdey-Heydorn, 2008).

A decision table was created using the cross-section profiles and trial-and-error method suggested by Erdey-Heydorn (2008). In addition, to assist in the determination of the threshold values, ten profiles (three were parallel to, and seven were transverse to the main axis of the WZFZ) were extracted from the DBM, slope and fine and broad- scale BPI layers (Figure 4, Supplementary Figure S3) for visual interpretation. Aspect and terrain ruggedness index (Vector Roughness Measurement) were also used to visualize and inform selection of threshold values (Figures 3, 4 and 5). Then BPI values and slope thresholds for all the structural classes were defined using expert judgement and adjusted to highlight each structural class after examination of cross-section profiles and several trial-and-error runs (Erdey-Heydorn, 2008) (Figure 4, Table 3). In this process, a natural threshold for slope angle was used to differentiate between flats (less than 6^{o}), Broad Slopes (between 6^{o} and

18^{o}), and Escarpments (more than 18^{o}). Flat regions appear along the axis of the fracture zone and the base of the tectonic highs; therefore, the 6000 m water depth threshold was used to differentiate Lower Plains (deeper than 6000 m) from the Terraces (shallower than 6000 m) (Figures 5a-b). Broad and fine scale BPI values display consistently low values for the central region and higher values for the tectonic highs (Figures 5b-c). This higher variability corresponds to stark changes in relief over the ridged area, indicating irregular bathymetry formed by a combination of crests and depressions associated with tectonic lineaments. A BPI of ±100 (equal to ±1 standard deviation) or its multiples (150 or 300) were used to define the thresholds for the structure classes (Hansen et al., 2022) (Figure 4, Table 3). The 6000 m water depth contour was again used to differentiate the Lower Troughs (deeper than 6000 m) in the central floor region from the Upper Troughs (shallower than 6000 m) in-between the tectonic highs (Figure 4, Table 3). Aspect ratio shows the Plains has a small size, but a frequent alteration in slope directions and tectonic highs display larger but less frequent variations in direction (Figure 5d). Terrain ruggedness value is lower and more homogeneous for the Plains, but higher and more diverse values for the Lower Troughs and both northern and southern tectonic highs (Figure 5e). Finally, the selected depth, broad and fine scale BPI and slope thresholds were used to divide the benthic structure into eight classes (Plains, Lower Troughs, Broad slopes, Escarpments, Terraces, Upper Troughs, Ridges, and Crests), and then zonal statistics (maximum, minimum, range, mean and standard deviation) were calculated for these eight structural classes based on values from the DBM by using the ArcGIS (v.10.8) Spatial Analyst toolbox (Figures 3 and 6).

2.3.2. Benthic habitat characterization

Substrate types along the transects were analysed from video footage collected during submersible dives. In total, six dives (WZFZ-LF1 - WZFZ-LF6) were conducted; however, video footage from dive WZFZ-LF1 was excluded from the analysis due to poor visibility of the seafloor. Seafloor habitat in this study was defined as a specific seafloor substrate that associated with different seafloor morphological structures, following the classification system proposed by Greene et al. (1999, 2007). Substrate classification was carried out for all sections of video data where the seafloor is clearly visible and when the submersible moves along the seabed. Therefore, the actual surveying time for each transect is less than the total surveying time. In total, approximately 594 minutes of video was analysed. First, the useable video for each transect was uploaded to EventMeasure (v.6.03) and was divided into sections based on their locations relative to previously identified structural classes, which constrains the depth, slope, and BPI values for each class (Supplementary Figure S4). As these structural classes range in size from tens of meters to several kilometres, they act as fundamentals for mesoscale level benthic habitats based on Greene et al. (1999, 2007). Subsequently, more detailed substrate interpretation (equal to the Class level in the benthic habitat hierarchy of Green et al. 1999) were assigned within each interval based on the occurrences and dominance (more than 80%) of soft sediments, gravels, nodules, rock fragments and outcropping bedrocks in that interval (Perez et al., 2017; Correa et al., 2022; Bond et al., 2023). Start and end times of each substrate occurrence and corresponding depth were recorded. End time corresponds with the change to a different seafloor substrate type. Due to the fine-scale variation of seafloor substrate observed in video data compared to the delineation of structural classes derived from MBES, a substrate type was assigned only if the changes were abrupt and remained consistently for at least 30 s (Correa et al., 2022). Seabed composition, bedrock facies (Subclass level in Green et al. 1999), and modifiers (such as bioturbation and sediment dusting percentage) for each substrate were also added to the substrate description table. Finally, the structural classes and substrate types were merged to generate deep-sea habitat classes along the submersible diving transects.

The CTD data collected during the lander deployments was processed using standard procedures incorporated within the SBE Data Processing Software (Sea-Bird Scientific, 2018) and post-corrected with calibration. The basic environmental conditions of the water column are included in Supplementary Figure S5. Only the average bottom conditions are included in the data analysis and to confirm AABW characteristics of the surveyed area. These bottom conditions were assigned to the habitat units coincident with lander sites.

2.3.5. Classification of fauna

All organisms visible on video footage collected using LF were assigned to a functional feeding group based on their behavioural and physical means of acquiring food. Video footage was interrogated using EventMeasure (v.6.03) software which facilitates the annotation of organisms. Functional feeding groups included: suspension feeder, suspension feeder (stalked), suspension feeder (branched), filter feeder, filter feeder (stalked), filter feeder (branched), deposit feeder, mobile predator, scavenger, and roaming generalist.

Abundance of organisms within each functional feeding group for each habitat type were square root transformed then normalised by dividing transformed abundance by the time (minutes) spent surveying that habitat type. This process provides a scalable comparison for the abundance and distribution of megafauna assemblages among habitat type and reduces data saturation from highly abundant organisms such as ophiuroids.

3. Results

3.1. Seafloor morphology and benthic structural classes

The surveyed area ranged in depth from 3800 to 6675 m. As with many other fracture zones, the WZFZ hosts a central elongated depression (deeper than 6000 m) that is up to 18 km wide (Figure 1c). The deepest point (6675 m, Figure 1c) of the surveyed area is located near the southern margin of the depression that comprises a relatively flat topography characterised by gentle slope angles <6° (Figures 6a-b). The 6000 m contour line closes to the southeast, whilst remaining open to the northwest, beyond the study area, suggesting the central depression will extend further along the same trend. The southern boundary of the central depression is bound by a prominent tectonic high trending parallel to the major axis of the fracture zone. North of the central depression is characterised by a series of north-northwest striking highs divided by relatively flat areas in-between. The morphological heterogeneity of the tectonic highs is expressed as variable slope angles, higher BPI and terrain ruggedness values with variable aspect directions compared to the central deep region. (Figure 6c-f).

The BTM classified seafloor geomorphology into eight classes (Figure 6, Table 4). The linear, central bathymetric low mainly consists of Plains (Class 1) and Lower Troughs (Class 2). In this region, Plains are encompassed by the Lower troughs. Both structural classes elongated parallel to the 6000 m contour (Figure 6). About 14.8% of the survey area was classified as Plains, and has the maximum depth of 6675 m, and mean depth of 6558 m. The Lower Trough covers 6.3% of the surveyed area and has a maximum depth of 6638 m (Table 4). Lower Troughs transit into Broad Slopes (Class 3) forming the transition between the axis of the WZFZ and the northern and southern tectonic highs with some locations classed as Escarpments (Class 4). Broad Slopes comprise more extensive inclined areas (29.8% of the study area) ranging from 6 to 18°, whereas the Escarpments class comprise more localised areas (3.2% study area) of increased gradients exceeding 18°. Broad Slopes has the greatest depth ranges varying from 6620 m to 4315 m (Figure 6, Table 4). A relatively narrow (0.8 km at narrowest, and 4 km at widest) Terrace (Class 5) appears adjacent to the northern edge of the Broad Slopes. Localised Terraces are also observed as small areas usually in close proximity to Broad Slopes and have been identified across both the northern and southern tectonic highs, accounting for 6.3% of the surveyed area (Figure 6, Table 4). Upper Troughs (Class 6) have the second largest coverage (22.3%) in the study area and occupies large regions between Ridges (Class 7) across the southern and northern tectonic highs. Ridges are depicted as areas of both high BPI values and geographically surrounded by zones comprising the Broad Slopes class representing the transition from ridge to the intervening Upper Troughs. They cover around 12.3% of the area. Ridges located on the tectonic high to the south of the WZFZ axis appear to trend NE-SW, while Ridges of the northern tectonic high comprise several smaller ridges separated by Upper Troughs although exhibit a similar trend to the larger ridges of the south. Crests (Class 8) appear as summit of the Ridges and have similar orientations. The Crests class are observed at the shallowest depths (3885 m) and account for about 4.9% of the study area (Figure 6, Table 4).

3.4. Seafloor substrates and habitats

Nine seafloor habitat units were recorded from the video footage along the submersible diving tracks. Two of the habitats were found within the 6000 m contour line, with the remaining seven observed across the southern and northern tectonic highs (Figure 7, Table 5). Apart from the Upper Trough, all other seven structural classes were ground-truthed during submersible transects (Supplementary Figure S4). The central floor region of the fracture zone, comprising benthic structural classes of Plains and Lower Troughs, is represented on video footage by Floor Sediments (FlrSed) habitat. FlrSed consisted of mixed soft mud and ooze. Bioturbation tracks prevailed in this habitat and had some (< 20%) coverage of xenophyophores. No indicators of seafloor currents such as ripples, or sediment waves were observed for this habitat (Figure 7a). CTD observations suggest that FlrSed habitat is dominated by AABW and has mean bottom temperature of 1.24 ˚C and salinity of 34.72 psu (practical salinity unit) (Table 5). This habitat was observed on the WZFZ-LF2 and WZFZ-LF3 dives and transited at the margins into Floor Debris (FlrDeb) habitat that was found mainly on WZFZ-LF3 and WZFZ-LF4 (Figures 6 and 7b). The FlrDeb unit comprised a soft mud-dominated matrix, with mixed gravels and boulders. The dark coloured gravels appeared poorly sorted and with sharp, angular edges (Figure 7b). This habitat was observed for around 64 minutes, and it likely has the same mean temperature and mean salinity as FlrSed. Slope Nodules (SlpNod) were the most dominant seascape observed, with a total of 274 minutes of observation during dives WZFZ-LF2, WZFZ-LF3, WZFZ-LF4, and WZFZ-LF5 (Figure 7c, Table 5 and 6). This unit is present across both southern and northern tectonic highs and occurred coincident with the benthic structural classes of Broad Slopes, Escarpments, and Terraces, with mean temperature of 1.22 ˚C and salinity of 34.72 psu (Figure 6, Table 5). In most cases, the seafloor comprised mud-rich soft substrate with nodules of different sizes and shapes (Figure 8). Some transects showed lobate-like, bedrock pavements underlying the nodules. The abundance of polymetallic nodules varied from <20% coverage (e.g. Figure 8a) to >90 % coverage (e.g. Figure 8c-e) of the seafloor. Occasionally, the nodules appear to have been transported downslope, suggesting not all the nodules had been formed in situ, but rather relocated from further up-slope by gravitational or hydrographic forces.

The upper segment of the Broad Slope structural class mainly comprised Slope Bedrock (SlpBed) habitat whereby smooth rocky outcrops with thin sediment veneer were observed on the video data (Figure 7d). The rocks are mainly volcanic and a potential pillow lava field was observed. The Slope Debris (SlpDeb) unit divided the SlpNod unit into two areas on transect of WZFZ-LF4 and were coincident with the Terraces benthic structural class of the southern tectonic high (Figure 7e, Table 5). SlpDeb habitat mainly consisted of basement pavement covered with a veneer of soft sediments, and patchy gravels of different sizes and angularity. The Rocky Ridge Walls (RigRock) and Ridge Wall Bedrocks (RigBed) habitat units were observed coincident with the Ridges benthic structural class. RigRock consisted of mixed sediments but mainly cobble and boulder sized fractions (Figure 7f, Table 5). Sands and gravels were observed locally within the fractures and local pockets between the rocky outcrops. RigBed had a comparatively smoother surface than RigRock, and the joints of bedrocks were clearly visible. Sands, gravel, and pebbles filled bedrock fractures and small terraces were observed locally, likely formed by downward transportation (Figure 7g, Table 5). Rocky Crests (CrsRock) and Crest Bedrock (CrsBed) habitats were observed in structural class areas defined as Crests. CrsRock consisted of poorly mixed gravel and pebbles (Figure 7h), while CrsBed mostly consisted of areas of exposed, clean bedrock that was not covered by gravel or a dusting of fine-grained sediments (Figure 7i, Table 5). RigRock, RigBed, CrsRock, and CrsBed were only recorded on dive WZFZ-LF2.

3.5. Distribution of organisms and functional feeding groups

A total of 498 organisms were scored from all submersible dives (Table 6). FlrSed had the highest abundance of organisms per minute of survey (3.90 ind. min^{-1}; Table 6) and CrsGran had the lowest abundance of organisms per minute of survey (0.27 ind. min^{-1}). Deposit feeders and Filter feeders were recorded across all seafloor habitats compared to Suspension feeders – branched which were only recorded in the FlrDeb, SlpNod, and SlpDeb units (Figure 9). RigRock had the lowest diversity of functional feeding groups (four) which included a notable absence of all forms of suspensions feeders. FlrDeb, SlpNod, and

SlpDeb were the only habitats which recorded all functional feeding groups, however, this observation is subjective as these seafloor habitats were sampled most during offshore data acquisition (Figure 9, Table 6).

Video footage from submersible dives shows variety in the assemblage of functional feeding groups and their association with the underlying habitat. As the submersible traversed the plains and troughs dominated by soft sediment, deposit-feeders were observed as the primary functional feeding group and accounted for approximately 75% of total standardised abundance in FlrSed (Figure 9). As the habitat transitioned into FlrDeb with an increase in pebbles and cobbles, the relative proportion of deposit feeders decreased, and the assemblage was dominated by suspension feeders. The assemblage of functional feeding groups at the SlpNod, SlpDeb, and SlpBed habitats were remarkably similar and heterogenous.

4. Discussion

4.1. Seafloor structures and habitat types

Analysis of new MBES data allowed for a detailed classification of seabed features and highlighted diverse seafloor structures and environment. Although other studies have utilised the BTM to characterise seafloor geomorphology and structure, most are applied to studies within shallow marine environments usually from the continental margin (Lecours et al., 2016; Lundblad et al., 2006; Walbridge et al., 2018; de Oliveira et al., 2020). This study represents one of the few that used this approach for structural classification of abyssal and hadal environments, where resolution is limited and there is increased topographic complexity (Perez et al., 2020; Corrêa et al., 2022). The application of the BTM and analysis of other terrain variables (aspect and ruggedness) have proved to be a powerful tool in delineating the morphological variations and distribution of classes in the deep-sea and the resultant geomorphological classes could be utilised as a surrogate for the occurrence of specific benthic fauna (Greene et al., 1999; Bowden et al., 2016; Mello-Rafter et al., 2021). High resolution bathymetric data tends to be more limited in the deep-sea and the amalgamated terrain attributes computed from the DBM enabled us to classify the seafloor into eight unique classes and quantitatively analyse their relationship and distribution (Figure 6, Table 4). Like many rifts, trenches and fracture zones, the axis of the WZFZ is characterised by an elongated flat plain surrounded by troughs which transition into broad slopes that separate the bathymetric low of the fracture zone axis from the tectonic highs topped with high relief ridges and crests that delineate the outer flanks of the structure (Jamieson et al., 2020, 2021; Perez et al., 2020).

The semi-automatic delineation of morphological features used in this study is of particular importance for bottom type evaluation and potential habitat prediction (Greene et al., 1999). Dive trajectories explored from the deep and relatively flat floor of the fracture zone to the ridge and crest of the tectonic highs. The topographic lows, flat-lying expanses of seabed, such Plains and Lower Troughs are more likely dominated by soft sediments with elevated regions such as Ridges and Crests dominated by outcropping rocks, contrasting with Slops that that can possess a complex combination of both sediments and bedrock (Narayanaswamy et al., 2013; Perez et al., 2020; Corrêa et al., 2022). Although, this relationship between substrate types and structural classes is supported here by video footage, the actual coverage of each habitat unit could not be constrained as more controlling points are needed and the purpose of this study is to investigate the influence of seabed structures and substrate types on the distribution of benthic functional groups. Each habitat unit examined in this study refers to a specific substrate type that observed within specific seabed structural class or combination of classes (Table 5). More robust, quantitative, and even fully automated seafloor habitat classification methods have been widely used in marginal and coastal waters where the resolution and quality of hydro-acoustic data (bathymetry and backscatter) are high; speed and accurate position of towed cameras and still images are well controlled and physical sampling is convenient for ground-truthing (Lecours et al., 2016; Lundblad et al., 2006; Porskamp et al., 2018, 2022). There remains significant challenges concerning the logistics and technical difficulties in the exploration of the deep-sea especially those in remote locations such as the WZFZ, with integrating broad scale bathymetric data with fine scale in situ observations of substrate types, our study provides a template for future studies to follow when attempting to combine geological and biological information for habitat characterisation purposes.

4.2. Polymetallic nodules

The polymetallic nodule field observed in this study represents one of the newest nodule fields in the Indian Ocean. Polymetallic nodules were observed coincident with regions classified as Broad and Steep Slopes, while the central floor area (Plains and Lower Troughs) was dominated by bioturbated soft sediments (FlrSed) and debris (FlrDeb). Polymetallic nodules, also known as ferromanganese nodules or manganese nodules, are composed of iron and manganese oxides that accumulate around a nucleus on the vast abyssal plains of the global ocean (Hein and Koschinsky, 2014; Kuhn et al., 2017; Hein et al., 2020). They form on top of, or within the first 10 cm of deep-sea sediments by the precipitation of manganese and iron oxides from seawater (hydrogenic nodules) or by early diagenetic processes (diagenetic nodules) (Hein et al., 1997; Konstantinova et al., 2017; Usui et al., 2017). They are often rich in a wide variety of metals such as nickel, cobalt, copper, titanium and rare earth elements. The Cape Leeuwin manganese nodule field lies on the northern flank of the Southeast Indian Ridge located in the southeast Indian Ocean (Kennett and Watkins, 1975, 1976; Frakes, 1982) (Figure 1a). Although its northern boundary is not clear, Frakes (1982) speculated that the nodule field could extend across the Diamantina Fracture Zone and into the Perth Abyssal Plain. Coincidently, some nodules up to 7 cm in diameter were found on the ridges of the WZFZ (Werner et al., 2017; Weston et al., 2020). By collating evidence from multiple sites, our study confirms and extends the area of the WZFZ nodule field while also raising questions regards its full range (Figures 7 and 8). Further investigation is required to understand if the WZFZ nodule field extends down the eastern side of the Indian Ocean and connects with the Cape Leeuwin nodule field.

A global assessment of nodule occurrences showed that low sedimentation rate is one of the key factors to promote nodule formation (Dutkiewicz et al., 2020). This may explain the absence of nodules in the Plain and Lower Trough area which are dominated by soft sediments suggesting the active deposition of fine-grained sediments (Dutkiewicz et al., 2020; Tagliaro et al., 2022). Video footage shows bioturbation of soft sediments across the Plains by benthic megafauna that may also have hindered the growth of nodules by redistributing seafloor particles (Banerjee, 2000). In addition, ferromanganese nodules and crust tend to grow preferentially on seamounts, slopes, and ridges, as they provide hard and commonly sediment-free substrates onto which they can precipitate (Halbach and Puteanus, 1984). As structural heterogeneity was also observed as an important factor in controlling the distribution of nodules (Pautot and Melguen, 1979; Mukhopadhyay and Ghosh, 2010), the alteration of ridges, troughs, terraces and slopes in the fracture zone likely have provided essential materials for the initiation of nodule growth.

In addition, the nodules on these slopes show significant variation in density and size (Figure 8). These differences in the presence, abundance, and sizes of nodules may have links to the availability of nucleating materials as well as seafloor characteristics. The formation of a nodule depends on the presence of any solid object as a seed upon which concentric layers of ferromanganese oxide precipitate and grow to form a nodule. Although, environmental conditions such as bottom-water characteristics, surface primary productivity, and total organic carbon content influence the presence and growth of polymetallic nodules (Mangini et al., 1990; Mukhopadhyay and Ghosh, 2010; Dutkiewicz et al., 2020). Bottom-water conditions in the study area are consistent with AABW (Supplementary material Figure S5 and S6), and there were no significant variations in bottom conditions observed for the areas with and without nodules (Vineesh et al., 2009) (Table 5). Primary productivity and total organic carbon are not varying substantially and dramatically from the polymetallic nodule dominated slopes to soft sediment dominated flat plains (Richardson et al., 2016). Therefore, the environmental conditions may have been related to the nodule formations on a regional scale but are not likely to be responsible for the localised presence and absence of nodules within the study area. Conversely, the difference in nucleus supply may explain differences in nodule sizes and concentrations. A positive relationship between high nodule abundance and the availability of rock fragments derived from seamounts and faults as nuclei has been observed in the eastern Pacific Ocean (Kuhn et al., 2017). Therefore, we suggest that fragmented rocks of various sizes spalling from upslope ridges and crests play an important role in the formation of the WZFZ nodules by providing seeds or cores for the nodules to grow.

4.3. Distribution of organisms and functional feeding groups

Habitat heterogeneity and species diversity are often positively related (Bowden et al., 2016; Collins et al., 2016; Stewart and Jamieson, 2018). The WZFZ is a heterogeneous environment across a variety of spatial scales; the WZFZ consists of varying morphologically defined classes (meso- or macro-habitats, *sensu* Green et al., 1999), including plains, troughs, slopes, terraces, ridges, and crests, which are further categorised into nine different habitat units based on seabed morphology, substrate types, and modifiers (Figure 6, Table 5). Despite having only classified organisms into functional feeding strategies, the differences in assemblage composition appears distinct amongst seafloor habitats. Seafloor habitats with a mixed heterogenous substrates and habitats (e.g., SlpNod, FlrDeb, and SlpDeb) that include soft sediment, cobbles/pebbles, and boulders have higher diversity of functional feeding groups utilising the complex array of physical structures (Figure 9). However, the density of organisms (and likely the time spent surveying a habitat) is important in defining the differences in functional traits amongst habitats, and more so than the presence/absence of individual traits (Hewitt et al., 2008). Interestingly, FlrSed and RigRock had the highest number of individuals per minute of survey (density; 3.90 and 1.07, respectively), yet both recorded low levels of diversity in functional feeding groups (five and four functional feeding groups, respectively). These differences in functional diversity amongst deep-sea habitats should be incorporated into any future development and implementation of conservation management strategies. Particularly when those habitats include fields of polymetallic nodules which we have demonstrated have diverse function of which we anticipate has limited redundancy at a species level (Schoening et al., 2020; Wear et al., 2021).

Depth is one of the primary determinants of marine biodiversity in the deep sea, as it correlates with physical characteristics of the water column such as temperature, oxygen, pressure, salinity, and organic matter. Although the study area spans the boundary between the abyssal and hadal zones, no dramatic change in bottom conditions was recorded and no clear variation was observed in functional groups with depth. Although this study only reports on a limited number of sample stations, we tentatively suggest that the seafloor morphology (as represented by benthic structural class) and substrate types are the major drivers in the assemblage of megafauna within the WZFZ. The abrupt changes in substrate types from the soft-sediment-dominated FlrSed to a more granular and pebble-covered FlrDeb coincides with the decline of deposition feeders from 75% to 25% and the addition of suspension feeders to the community structure. The uneven distribution of rock fragments and occasionally observed boulders are likely utilised by the suspension feeders to sustain themselves and exploit the suspended food particles. Hard substrates located on the slope (SlpDeb, SlpBed and SlpNod) provide more heterogeneous habitats compared to the soft sediment, and more diverse community groups were associated with them.

5. Conclusion

High-resolution MBES data have shown great value in mapping seabed geomorphological features and characterising substrate domains. Studying deep-sea geomorphology, substrate domain, and the distribution of organism function is challenging because of the limited access to study in detail these ultra-deep ecosystems. By adopting a nested approach that integrated the broad-scale morphological features of the Wallaby-Zenith Fracture Zone in the East Indian Ocean, with fine-scale observations of substrate types and records of function groups of benthic fauna we have developed a template for future studies to follow when attempting to combine geological and biological information for habitat characterisation purposes. The study area could be classified into eight structural classes, and nine habitat units based on their bathymetric derivatives and substrate types as interpreted from submersible video footage. We observed a polymetallic nodule field that the availability of rock fragments as nuclei combined with seafloor topography are the primary drivers for the formation of the nodules. This work marks the first detailed study of this extension of the Cape Leeuwen nodule field. The occurrence of hard substrate, particularly the polymetallic nodules on the slopes, facilitated the functional diversity of the benthic fauna.

Acknowledgements

We thank the funders of expedition "Indomitable" which was a joint mission between Caladan Oceanic LLC (USA) and the Minderoo Foundation (Australia). We thank submersible pilots Tim Macdonald and Shane Eigler (Caladan Oceanic LLC) and their co-pilots AJJ and Alan Scott. We thank the captain, crew, and company of the DSSV *Pressure Drop*, EYOS Expeditions, and the submersible support team at Caladan Oceanic LLC and Triton Submarines (USA). Cassandra Bongiovanni, Jaya Roperez, Roxy Wrigley, and Nelson Kuna are thanked for their support and suggestions during the acquisition and processing of the MBES data. The analysis and writing of this study were supported by the Minderoo-UWA Deep-Sea Research Centre, funded by the Minderoo Foundation. HAS publishes with the permission of the Executive Director of the British Geological Survey (United Kingdom Research and Innovation).

References

Banerjee, R., 2000. A documentation on burrows in hard substrates of ferromanganese crusts and associated soft sediments from the Central Indian Basin. Curr. Sci. 79, 517–521.

Bird, D., 2001. Shear margins Continent-ocean transform and fracture zone boundaries. The Leading Edge, 20(2), 150-159. https://doi.org/10.1190/1.1438894

Bond, T., Niyazi, Y., Kolbusz, J.L., Jamieson, A.J., 2023. Habitat and benthic fauna of the Wallaby-Cuvier escarpment, SE Indian ocean. Deep Sea Res. Part 2 Top. Stud. Oceanogr. 210, 105299. https://doi.org/10.1016/j.dsr2.2023.105299

Bongiovanni, C., Stewart, H.A., Jamieson, A.J., 2022. High-resolution multibeam sonar bathymetry of the deepest place in each ocean. Geoscience Data Journal, Vol. 9(1), 108–123. https://doi.org/10.1002/gdj3.122

Bowden, D.A., Rowden, A.A., Leduc, D., Beaumont, J., Clark, M.R., 2016. Deep-sea seabed habitats: Do they support distinct mega-epifaunal communities that have different vulnerabilities to anthropogenic disturbance? Deep Sea Res. Part I 107, 31–47. https://doi.org/10.1016/j.dsr.2015.10.011

Collins, D.L., Langlois, T.J., Bond, T., Holmes, T.H., Harvey, E.S., Fisher, R., McLean, D.L., 2017. A novel stereo-video method to investigate fish–habitat relationships. Methods Ecol. Evol. 8, 116–125. https://doi.org/10.1111/2041-210X.12650

Corrêa, P.V.F., Jovane, L., Murton, B.J., Sumida, P.Y.G., 2022. Benthic megafauna habitats, community structure and environmental drivers at Rio Grande Rise (SW Atlantic). Deep Sea Res. Part I 186, 103811. https://doi.org/10.1016/j.dsr.2022.103811

Daniell, J., Jorgensen, D.C., Anderson, T., Borissova, I., Burq, S., Heap, A., Hughes, M., Mantle, D., Nelson, G., Nichol, S., Nicholson, C., Payne, D., Przeslawski, R., Radke, L., Siqabessy, J., Smith, C., Shipboard Party, 2009. Frontier basins of the West Australian Continental Margin: Post-survey report of marine reconnaissance and geological sampling survey GA2476. Geosci. Aust, Record 2009/38, 229pp.

Dartnell, P., Gardner, J.V., 2004. Predicting Seafloor Facies from Multibeam Bathymetry and Backscatter Data. Photogrammetric Engineering & Remote Sensing 70, 1081–1091. https://doi.org/10.14358/PERS.70.9.1081

Davies, J.S., Stewart, H.A., Narayanaswamy, B.E., Jacobs, C., Spicer, J., Golding, N., Howell, K.L., 2015. Benthic Assemblages of the Anton Dohrn Seamount (NE Atlantic): Defining Deep-Sea Biotopes to Support Habitat Mapping and Management Efforts with a Focus on Vulnerable Marine Ecosystems. PLOS ONE. https://doi.org/10.1371/journal.pone.0124815

de Oliveira, N., Bastos, A.C., da Silva Quaresma, V., Vieira, F.V., 2020. The use of Benthic Terrain Modeler (BTM) in the characterisation of continental shelf habitats. Geo-Mar. Lett. 40, 1087–1097. https://doi.org/10.1007/s00367-020-00642-y

Dutkiewicz, A., Judge, A., Dietmar Müller, R., 2020. Environmental predictors of deep-sea polymetallic nodule occurrence in the global ocean. Geology 48, 293–297. https://doi.org/10.1130/G46836.1

Erdey-Heydorn, M.D., 2008. An ArcGIS Seabed Characterization Toolbox Developed for Investigating Benthic Habitats. Mar. Geod. 31, 318–358. https://doi.org/10.1080/01490410802466819

Fox, P.J., Schreiber, E., Rowlett, H., McCamy, K., 1976. The geology of the Oceanographer Fracture Zone: a model for fracture zones. Journal of Geophysical Research, 81(23), 4117-4128. https://doi.org/10.1029/JB081i023p04117

Frakes, L.A., 1982. Metal chemistry of manganese nodules from the Cape Leeuwin field, southeast Indian Ocean. Mar. Geol. 47, M1–M10. https://doi.org/10.1016/0025-3227(82)90014-7

GEBCO Compilation Group (2022) GEBCO_2022 Grid (doi:10.5285/e0f0bb80-ab44-2739-e053-6c86abc0289c)

Gibbons, A.D., Barckhausen, U., van den Bogaard, P., Hoernle, K., Werner, R., Whittaker, J.M., Müller, R.D., 2012. Constraining the Jurassic extent of Greater India: Tectonic evolution of the West Australian margin. Geochem. Geophys. Geosyst. 13. https://doi.org/10.1029/2011gc003919

Gordon, A.L., Tchernia, P.L., 1978. Waters of the continental margin off Adélie Coast, Antarctica, in: Antarctica Oceanology II: The Australian—New Zealand Sector, Antarctic Research Series. American Geophysical Union, Washington, D. C., pp. 59–69. https://doi.org/10.1029/ar019p0059

Greene, H.G., Yoklavich, M.M., Starr, R.M., O'Connell, V.M., Wakefield, W.W., Sullivan, D.E., McRea, J.E., Cailliet, G.M., 1999. A classification scheme for deep seafloor habitats. Oceanol. Acta 22, 663–678. https://doi.org/10.1016/S0399-1784(00)88957-4

Greene, H.G., Bizzarro, J.J., O'Connell, V.M., and Brylinsky, C.K., 2007. Construction of digital potential marine benthic habitat maps using a coded classification scheme and its application, in Todd, B.J., and Greene, H.G., eds., Mapping the Seafloor for Habitat Characterization: Geological Association of Canada, Special Paper 47, p. 141-155.

Halbach, P., Puteanus, D., 1984. The influence of the carbonate dissolution rate on the growth and composition of Co-rich ferromanganese crusts from Central Pacific seamount areas. Earth Planet. Sci. Lett. 68, 73–87. https://doi.org/10.1016/0012-821X(84)90141-9

Harff, J., Meschede, M., Petersen, S., Thiede, J. (Eds.), 2016. Encyclopedia of marine geosciences, Encyclopedia of Earth Sciences Series. Springer, Dordrecht, Heidelberg.

Harris, P., Baker, E., 2011. Seafloor Geomorphology as Benthic Habitat: GeoHAB Atlas of Seafloor Geomorphic Features and Benthic Habitats. Elsevier.

Harris, P.T., Macmillan-Lawler, M., Rupp, J., Baker, E.K., 2014. Geomorphology of the oceans. Mar. Geol. 352, 4–24. https://doi.org/10.1016/j.margeo.2014.01.011

Helland-Hansen, B, 1916. Nogen hydrografiske metoder. Naturforsker Möte, Kristiania.

Heezen, B.C., Gerard, R.D., Tharp, M., 1964. The Vema fracture zone in the equatorial Atlantic. Journal of Geophysical Research, 69(4), pp.733-739. https://doi.org/10.1029/JZ069i004p00733

Hein, J.R., Koschinsky, A., 2014. Deep-ocean ferromanganese crusts and nodules, in: Treatise on Geochemistry. Elsevier, pp. 273–291. https://doi.org/10.1016/b978-0-08-095975-7.01111-6

Hein, J.R., Koschinsky, A., Kuhn, T., 2020. Deep-ocean polymetallic nodules as a resource for critical materials. Nature Reviews Earth & Environment 1, 158–169. https://doi.org/10.1038/s43017-020-0027-0

Hein, J.R., Mizell, K., Koschinsky, A., Conrad, T.A., 2013. Deep-ocean mineral deposits as a source of critical metals for high- and green-technology applications: Comparison with land-based resources. Ore Geol. Rev. 51, 1–14.

Hewitt, J.E., Thrush, S.F., Dayton, P.D., 2008. Habitat variation, species diversity and ecological functioning in a marine system. J. Exp. Mar. Bio. Ecol. 366, 116–122. https://doi.org/10.1016/J.JEMBE.2008.07.016

IHO, 2008. Standardisation of Undersea Feature Names: Guidelines Proposal form Terminology, 4th ed. International Hydrographic Organisation and Intergovernmental Oceanographic Commission, Monaco.

IOC, SCOR, IAPSO, 2010. The international thermodynamic equation of seawater—2010: Calculations and use of thermodynamic properties. Intergovernmental Oceanographic Commission, Manuals and Guides No. 56, UNESCO, pp. 1–196.

Jacob, J., Dyment, J., Yatheesh, V., 2014. Revisiting the structure, age, and evolution of the Wharton Basin to better understand subduction under Indonesia. J. Geophys. Res: Solid Earth. 119, 169–190. https://doi.org/10.1002/2013jb010285

Jamieson, A.J., Stewart, H.A., Rowden, A.A., Clark, M.R., 2020. Chapter 59 – Geomorphology and benthic habitats of the Kermadec Trench, Southwest Pacific Ocean, in: Harris, P.T., Baker, E. (Eds.), Seafloor Geomorphology as Benthic Habitat (Second Edition). Elsevier, pp. 949–966. https://doi.org/10.1016/B978-0-12-814960-7.00059-2

Jamieson, A.J., Stewart, H.A., Weston, J.N.J., Bongiovanni, C., 2021. Hadal fauna of the South Sandwich Trench, Southern Ocean: Baited camera survey from the Five Deeps Expedition. Deep Sea Res. Part 2 Top. Stud. Oceanogr. 194, 104987. https://doi.org/10.1016/j.dsr2.2021.104987

Jamieson, A.J., Stewart, H.A., Weston, J.N.J., Lahey, P., Vescovo, V.L., 2022. Hadal Biodiversity, Habitats and Potential Chemosynthesis in the Java Trench, Eastern Indian Ocean. Frontiers in Marine Science 9. https://doi.org/10.3389/fmars.2022.856992

Kennett, J.P., Watkins, N.D., 1976. Regional deep-sea dynamic processes recorded by late Cenozoic sediments of the southeastern Indian Ocean. GSA Bulletin 87, 321–339. https://doi.org/10.1130/0016-7606(1976)87<321:RDDPRB>2.0.CO;2

Kennett, J.P., Watkins, N.D., 1975. Deep-sea erosion and manganese nodule development in the southeast Indian ocean. Science 188, 1011–1013. https://doi.org/10.1126/science.188.4192.1011

Konstantinova, N., Cherkashov, G., Hein, J.R., Mirão, J., Dias, L., Madureira, P., Kuznetsov, V., Maksimov, F., 2017. Composition and characteristics of the ferromanganese crusts from the western Arctic Ocean. Ore Geol. Rev. 87, 88–99. https://doi.org/10.1016/j.oregeorev.2016.09.011

Kuhn, T., Wegorzewski, A., Rühlemann, C., Vink, A., 2017. Composition, Formation, and Occurrence of Polymetallic Nodules, in: Sharma, R. (Ed.), Deep-Sea Mining: Resource Potential, Technical and Environmental Considerations. Springer International Publishing, Cham, pp. 23–63. https://doi.org/10.1007/978-3-319-52557-0_2

Lecours, V., Dolan, M.F.J., Micallef, A., Lucieer, V.L., 2016. A review of marine geomorphometry, the quantitative study of the seafloor. Hydrol. Earth Syst. Sci. 20, 3207–3244. https://doi.org/10.5194/hess-20-3207-2016

Longhurst, A., Sathyendranath, S., Platt, T., Caverhill, C., 1995. An estimate of global primary production in the ocean from satellite radiometer data. Journal of Plankton Research. https://doi.org/10.1093/plankt/17.6.1245Lundblad, E.R., Wright, D.J., Miller, J., Larkin, E.M., Rinehart, R., Naar, D.F., Donahue, B.T., Anderson, S.M., Battista, T., 2006. A Benthic Terrain Classification Scheme for American Samoa. Mar. Geod. 29, 89–111. https://doi.org/10.1080/01490410600738021

Lurton, X., 2010. An Introduction to Underwater Acoustics. Springer Berlin Heidelberg.

Mammerickx, J. and Sandwell, D., 1986. Rifting of old oceanic lithosphere. Journal of Geophysical Research: Solid Earth, 91(B2), pp.1975-1988. https://doi.org/10.1029/JB091iB02p01975

Mangini, A., Eisenhauer, A., Walter, P., n.d. Response of manganese in the ocean to the climatic cycles in the Quaternary. Paleoceanography. https://doi.org/10.1029/PA005i005p00811

Mantyla, A.W., Reid, J.L., 1995. On the origins of deep and bottom waters of the Indian Ocean. J. Geophys. Res. 100, 2417. https://doi.org/10.1029/94jc02564Marghany, M., Mansor, S., Shariff, A.R.B., 2016. Genetic algorithm for investigating flight MH370 in Indian Ocean using remotely sensed data. IOP Conf. Ser.: Earth Environ. Sci. 37, 012001. https://doi.org/10.1088/1755-1315/37/1/012001

McGonigle, C., Collier, J.S., 2014. Interlinking backscatter, grain size and benthic community structure. Estuar. Coast. Shelf Sci. 147, 123–136. https://doi.org/10.1016/j.ecss.2014.05.025

Mello-Rafter, K., Sowers, D., Malik, M., Watling, L., Mayer, L.A., Dijkstra, J.A., 2021. Environmental and Geomorphological Effects on the Distribution of Deep-Sea Canyon and Seamount Communities in the Northwest Atlantic. Frontiers in Marine Science 8. https://doi.org/10.3389/fmars.2021.691668

Menard, H.W., Atwater, T., 1969. Origin of fracture zone topography. Nature, 222(5198), 1037-1040. 1037–1040. https://doi.org/10.1038/2221037a0

Mercier, H., Morin, P., 1997. Hydrography of the Romanche and Chain fracture zones. Journal of Geophysical Research: Oceans, 102(C5), pp.10373-10389. https://doi.org/10.1029/97JC00229

Nanson, R., Arosio, R., Gafeira, J., McNeil, M., Dove, D., Bjarnadóttir, L., Dolan, M.F.J., Guinan, J., Post, A., Webb, J. Nichol, S. 2022. A two-part seabed geomorphology classification scheme. Part 2: Geomorphology classification framework and glossary – Version 1.0. Published 14th April 2023. DOI: 10.5281/zenodo.7804019

Narayanaswamy, B.E., Hughes, D.J., Howell, K.L., Davies, J., Jacobs, C., 2013. First observations of megafaunal communities inhabiting George Bligh Bank, Northeast Atlantic. Deep Sea Res. Part 2 Top. Stud. Oceanogr. 92, 79–86. https://doi.org/10.1016/j.dsr2.2013.03.004

Mukhopadhyay, R., Ghosh, A.K., 2010. Dynamics of formation of ferromanganese nodules in the Indian Ocean. J. Asian Earth Sci. 37 (4), 394-398.https://doi.org/10.1016/j.jseaes.2009.09.003

Nelson, G., Hughes, M., Przeslawski, R., Nichol, S., Lewis, B., 2009. Revealing the Wallaby Plateau: Recent survey delivers geophysical, geological and biophysical data. AusGeo news.

Olierook, H.K.H., Merle, R.E., Jourdan, F., Sircombe, K., Fraser, G., Timms, N.E., Nelson, G., Dadd, K.A., Kellerson, L., Borissova, I., 2015. Age and geochemistry of magmatism on the oceanic Wallaby Plateau and implications for the opening of the Indian Ocean. Geology 43, 971–974. https://doi.org/10.1130/G37044.1

Pautot, G., Melguen, M., 1979. Influence of Deep Water Circulation and Sea Floor Morphology on the Abundance and Grade of Central South Pacific Manganese Nodules, in: Bischoff, J.L., Piper, D.Z. (Eds.), Marine Geology and Oceanography of the Pacific Manganese Nodule Province. Springer US, Boston, MA, pp. 621–649. https://doi.org/10.1007/978-1-4684-3518-4_18

Perez, J.A.A., Gavazzoni, L., de Souza, L.H.P., Sumida, P.Y.G., Kitazato, H., 2020. Deep-Sea Habitats and Megafauna on the Slopes of the São Paulo Ridge, SW Atlantic. Frontiers in Marine Science 7. https://doi.org/10.3389/fmars.2020.572166

Picard, K., Brooke, B.P., Harris, P.T., Siwabessy, P.J.W., Coffin, M.F., Tran, M., Spinoccia, M., Weales, J., Macmillan-Lawler, M., Sullivan, J., 2018. Malaysia Airlines flight MH370 search data reveal geomorphology and seafloor processes in the remote southeast Indian Ocean. Mar. Geol. 395, 301–319. https://doi.org/10.1016/j.margeo.2017.10.014.

Porskamp, P., Rattray, A., Young, M., Ierodiaconou, D., 2018. Multiscale and Hierarchical Classification for Benthic Habitat Mapping. Geosci. J. 8, 119. https://doi.org/10.3390/geosciences8040119

Porskamp, P., Young, M., Rattray, A., Brown, C.J., Hasan, R.C., Ierodiaconou, D., 2022. Integrating Angular Backscatter

Response Analysis Derivatives Into a Hierarchical Classification for Habitat Mapping. Frontiers in Remote Sensing 3. https://doi.org/10.3389/frsen.2022.903133

Richardson, K., Bendtsen, J., Kragh, T., Mousing, E.A., 2016. Constraining the Distribution of Photosynthetic Parameters in the Global Ocean. Frontiers in Marine Science 3. https://doi.org/10.3389/fmars.2016.00269

Riehl, T., Wölfl, A.-C., Augustin, N., Devey, C.W., Brandt, A., 2020. Discovery of widely available abyssal rock patches reveals overlooked habitat type and prompts rethinking deep-sea biodiversity. Proc. Natl. Acad. Sci. U. S. A. 117, 15450–15459. https://doi.org/10.1073/pnas.1920706117

Rochford, J., 1966. Distribution of Banda Intermediate Water in the Indian Ocean. Australian Journal of Marine and Freshwater Research, 17, 61–76.

Sea-Bird Scientific, 2020. SBE 49 FastCAT CTD Sensor User Manual (Manual No. 018). https://www.seabird.com/sbe-49-fastcat-ctd/product-downloads?id=60762467704

Schimel, A.C.G., Beaudoin, J., Parnum, I.M., Le Bas, T., Schmidt, V., Keith, G., Ierodiaconou, D., 2018. Multibeam sonar backscatter data processing. Mar. Geophys. Res. 39, 121–137. https://doi.org/10.1007/s11001-018-9341-z

Schoening, T., Purser, A., Langenkämper, D., Suck, I., Taylor, J., Cuvelier, D., Lins, L., Simon-Lledó, E., Marcon, Y., Jones, D.O.B., Nattkemper, T., Köser, K., Zurowietz, M., Greinert, J., Gomes-Pereira, J., 2020. Megafauna community assessment of polymetallic-nodule fields with cameras: platform and methodology comparison. Biogeosciences 17, 3115–3133. https://doi.org/10.5194/bg-17-3115-2020

Shuhail, M., Yatheesh, V., Bhattacharya, G.C., Müller, R.D., Raju, K.K. and Mahender, K., 2018. Formation and evolution of the Chain-Kairali Escarpment and the Vishnu Fracture Zone in the western Indian Ocean. Journal of Asian Earth Sciences, 164, pp.307-321. https://doi.org/10.1016/j.jseaes.2018.06.022

Smith, W.H.F., Sandwell, D.T., 1997. Global Sea Floor Topography from Satellite Altimetry and Ship Depth Soundings. Science 277, 1956–1962. https://doi.org/10.1126/science.277.5334.1956

Stefanoudis, P., Talma, S., Samimi-Namin, K., Woodall, L., 2020. Deep reef ecosystems of the Western Indian Ocean: addressing the great unknown. Res. Ideas Outcomes 6. https://doi.org/10.3897/rio.6.e53913

Stewart, H.A., Jamieson, A.J., 2019. The five deeps: The location and depth of the deepest place in each of the world's oceans. Earth-Sci. Rev. 197, 102896. https://doi.org/10.1016/j.earscirev.2019.102896

Stewart, H.A., Jamieson, A.J., 2018. Habitat heterogeneity of hadal trenches: Considerations and implications for future studies. Prog. Oceanogr. 161, 47–65. https://doi.org/10.1016/j.pocean.2018.01.007

Swanborn, D.J.B., Huvenne, V.A.I., Pittman, S.J., Rogers, A.D., Taylor, M.L., Woodall, L.C., 2022. Mapping, quantifying and comparing seascape heterogeneity of Southwest Indian Ridge seamounts. Landscape Ecology. https://doi.org/10.1007/s10980-022-01541-6

Talley, L.D., Pickard, G.L., Emery, W.J., Swift, J.H., 2011. Descriptive physical oceangraphy: An introduction. Academic Press. https://doi.org/10.1016/C2009-0-24322-4

Talley, L. D., 2013. Hydrographic Atlas of the World Ocean Circulation Experiment (WOCE) Volume 4: Indian Ocean. eScholarship, University of California.

Tucholke, B.E., Schouten, H., 1988. Kane fracture zone. Marine Geophysical Researches, 10(1), 1-39. https://doi.org/10.1007/BF02424659

Uhlenkott, K., Meyn, K., Vink, A. et al. A review of megafauna diversity and abundance in an exploration area for polymetallic nodules in the eastern part of the Clarion Clipperton Fracture Zone (North East Pacific), and implications for potential future deep-sea mining in this area. Mar. Biodivers. 53, 22 (2023). https://doi.org/10.1007/s12526-022-01326-9

Usui, A., Nishi, K., Sato, H., Nakasato, Y., Thornton, B., Kashiwabara, T., Tokumaru, A., Sakaguchi, A., Yamaoka, K., Kato, S., Others, 2017. Continuous growth of hydrogenetic ferromanganese crusts since 17 Myr ago on Takuyo-Daigo Seamount, NW Pacific, at water depths of 800--5500 m. Ore Geol. Rev. 87, 71–87.

Vineesh, T.C., Nagender Nath, B., Banerjee, R., Jaisankar, S., Lekshmi, V., 2009. Manganese nodule morphology as indicators for oceanic processes in the Central Indian Basin. International Geology Review. https://doi.org/10.1080/00206810802622773

Wafar, M., Venkataraman, K., Ingole, B., Ajmal Khan, S., Lokabharathi, P., 2011. State of knowledge of coastal and marine biodiversity of Indian Ocean countries. PLoS One 6, e14613. https://doi.org/10.1371/journal.pone.0014613

Walbridge, S., Slocum, N., Pobuda, M., Wright, D.J., 2018. Unified Geomorphological Analysis Workflows with Benthic Terrain Modeler. Geosci. J. 8, 94. https://doi.org/10.3390/geosciences8030094

Wang, M., Wu, Z., Best, J., Yang, F., Li, X., Zhao, D., Zhou, J., 2021. Using multibeam backscatter strength to analyze the distribution of manganese nodules: A case study of seamounts in the Western Pacific Ocean. Appl. Acoust. 173, 107729. https://doi.org/10.1016/j.apacoust.2020.107729

Wear, E.K., Church, M.J., Orcutt, B.N., Shulse, C.N., Lindh, M.V., Smith, C.R., 2021. Bacterial and Archaeal Communities in Polymetallic Nodules, Sediments, and Bottom Waters of the Abyssal Clarion-Clipperton Zone: Emerging Patterns and Future Monitoring Considerations. Frontiers in Marine Science. https://doi.org/10.3389/fmars.2021.634803

Werner R, Wagner HJ, Hauff F (2017) RV SONNE Fahrtbericht/Cruise report SO258/1: INGON: The Indian - Antarctic Break-up Engima, Fremantle (Australia) - Colombo (Sri Lanka) 07.06.–09.07.2017. GEOMAR Report, N. Ser. 038. GEOMAR Helmholtz-Zentrum für Ozeanforschung Kiel, Kiel. https://doi.org/10.3289/GEOMAR_REP_NS_38_2017. Accessed 10 Aug 2022

Weston, J.N.J., Peart, R.A., Jamieson, A.J., 2020. Amphipods from the Wallaby-Zenith Fracture Zone, Indian Ocean: new genus and two new species identified by integrative taxonomy. System. Biodivers. 18, 57–78. https://doi.org/10.1080/14772000.2020.1729891

Weston, J.N.J., Peart, R.A., Stewart, H.A., Ritchie, H., Piertney, S.B., Linley, T.D., Jamieson, A.J., 2021. Scavenging amphipods from the Wallaby-Zenith Fracture Zone: Extending the hadal paradigm beyond subduction trenches. Mar. Biol. 168, 1. https://doi.org/10.1007/s00227-020-03798-4

Wolff, G.A., Billett, D.S.M., Bett, B.J., Holtvoeth, J., FitzGeorge-Balfour, T., Fisher, E.H., Cross, I., Shannon, R., Salter, I., Boorman, B., King, N.J., Jamieson, A., Chaillan, F., 2011. The effects of natural iron fertilisation on deep-sea ecology: the Crozet Plateau, Southern Indian Ocean. PLoS One 6, e20697. https://doi.org/10.1371/journal.pone.0020697

Zeppilli, D., Pusceddu, A., Trincardi, F., Danovaro, R., 2016. Seafloor heterogeneity influences the biodiversity–ecosystem functioning relationships in the deep sea. Scientific Reports. https://doi.org/10.1038/srep26352

Figures

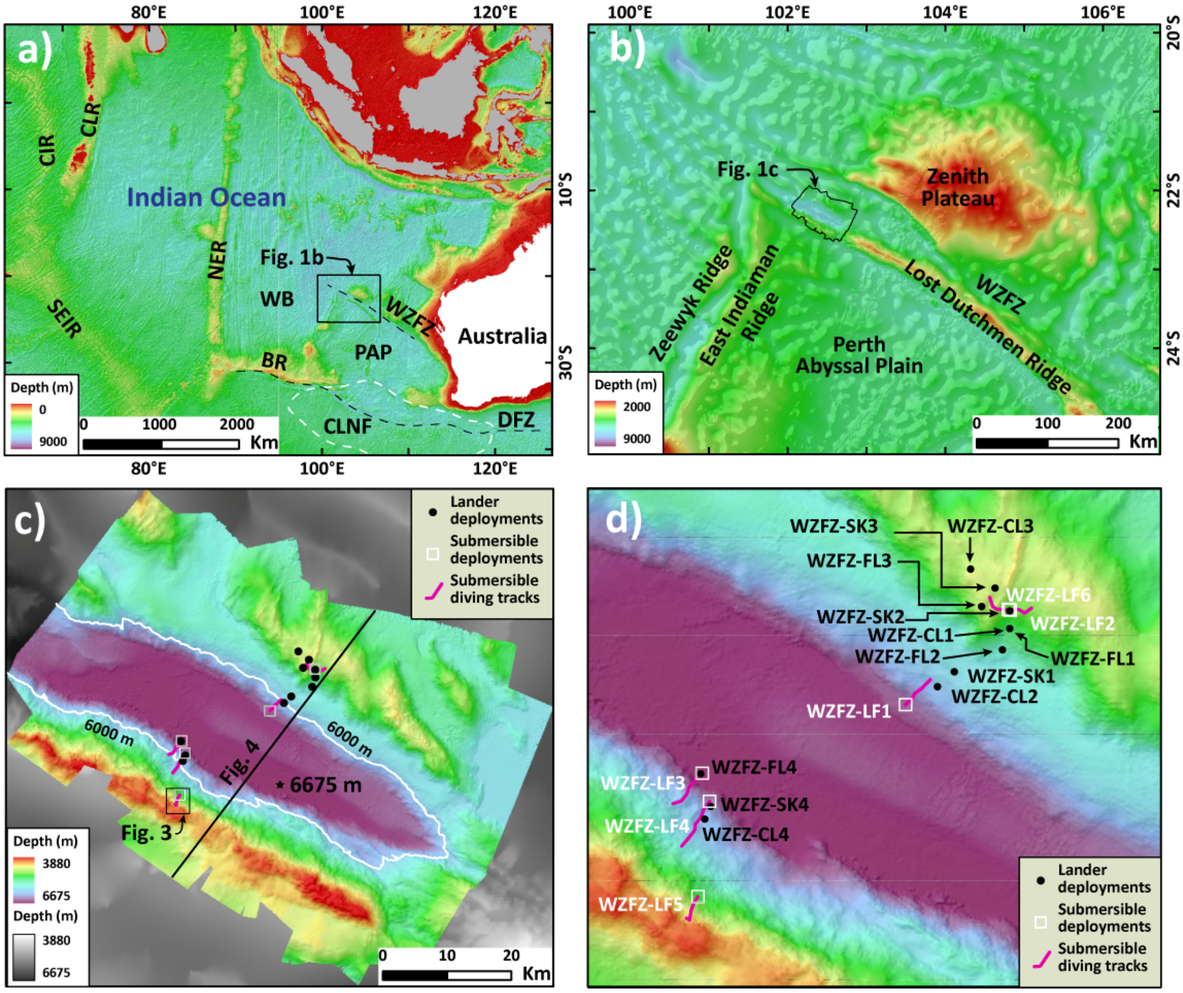

Figure 1. Location of the Wallaby-Zenith Fracture Zone (WZFZ) and study area. (a) Bathymetry and major morphological features of East Indian Ocean, based on GEBCO_2023 Grid (GEBCO Compilation Group, 2023). White dashed polygon represents the approximate extension of Cape Leeuwin Nodule Field (CLNF, complied from Frakes, 1982). BR: Broken Ridge, CIR: Central Indian Ridge, CLR: Chagos-Laccadive Ridge, DFZ: Diamantina Fracture Zone, NER: Ninety East Ridge, SEIR: Southeast Indian Ridge, WB: Wharton Basin. Feature names adhere to the International Hydrographic Organisation's nomenclature for geomorphic features (IHO, 2013). (c) Hillshade bathymetry based on new multibeam echosounder data (colour) overlaid on GEBCO_2023 Grid (greyscale). Star represents the deepest point identified within the surveyed area. (d) Zoom in map of the deployed scientific landers and submersible diving tracks.

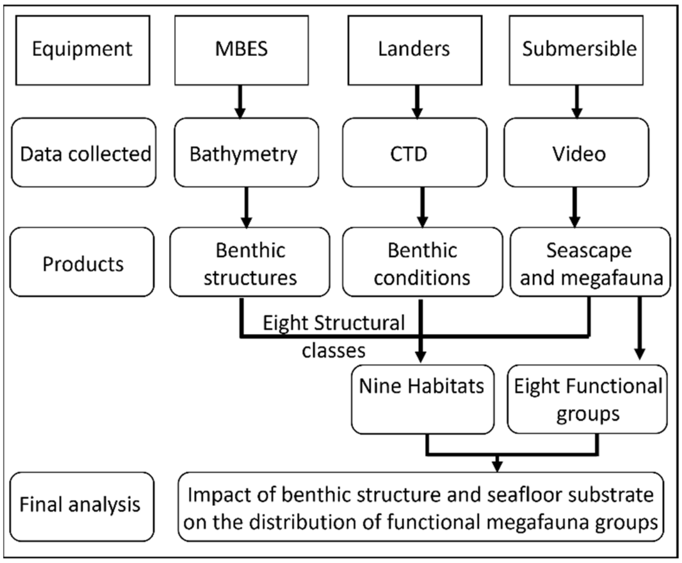

Figure 2. General chart showing main equipment, collected data, processed data and integrated final analysis in this research.

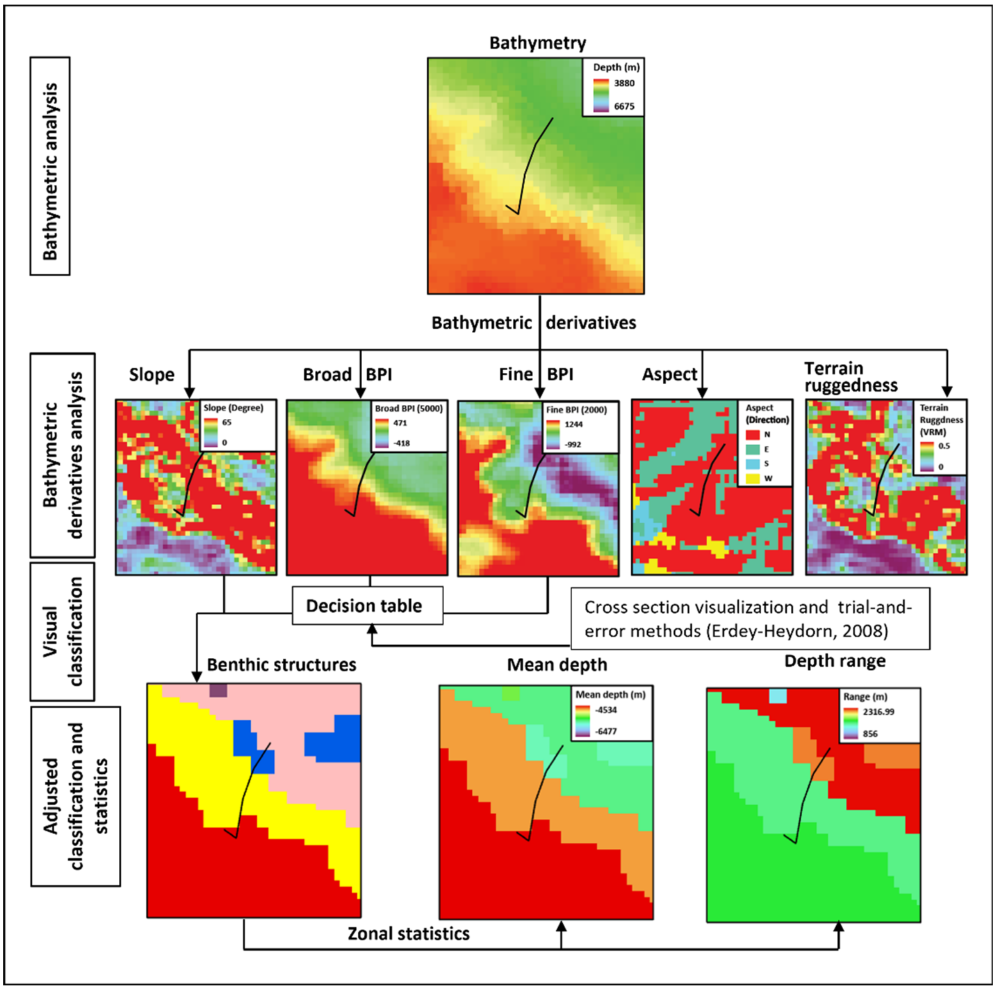

Figure 3. Workflow diagram showing the seafloor structural classification procedure applied to the Wallaby-Zenith Fracture Zone multibeam bathymetry (for geographical position please refer to Fig. 1c). Structural classification includes the analysis of depth and depth-derived terrain variables, visual classification, construction of a decision table and adjusted classification using the Benthic Terrain Modeler (BTM). The structural classes were converted from raster cells into polygons and zonal statistics (maximum, minimum, mean, median and standard deviation) were calculated based on values from the bathymetry.

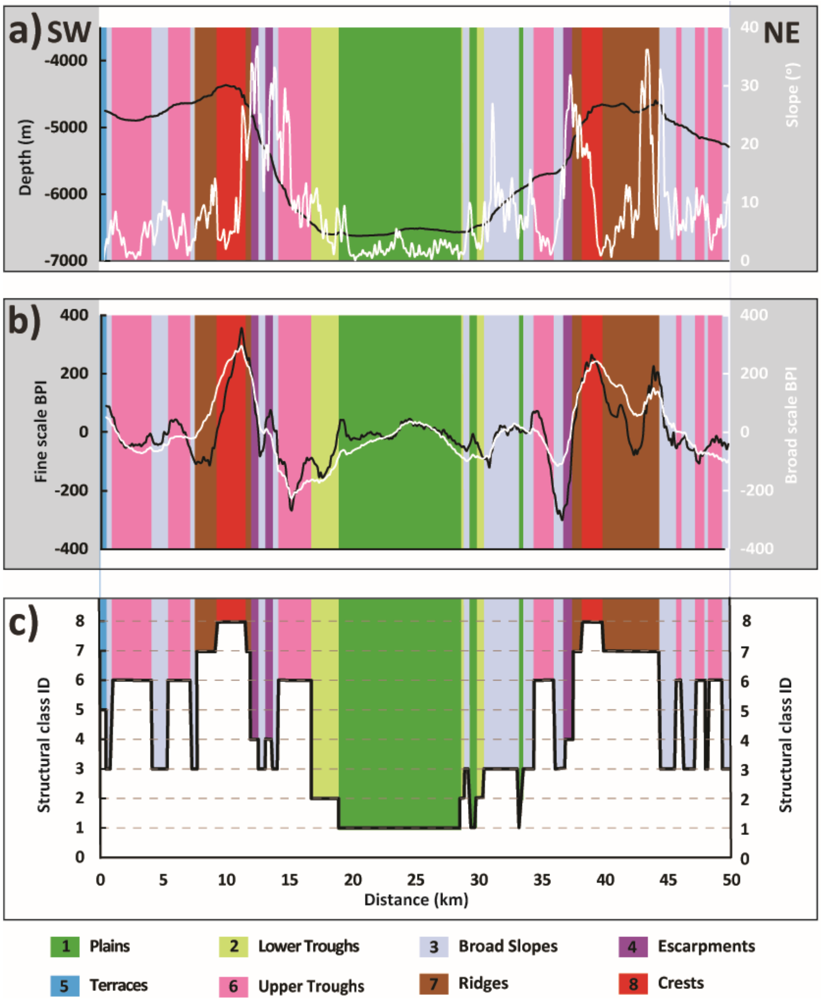

Figure 4. Cross sectional visualization of (a) depth and slope, (b) broad scale BPI (Bathymetric Position Index) and fine scale BPI, and their correlation with the (c) identified structural classes.

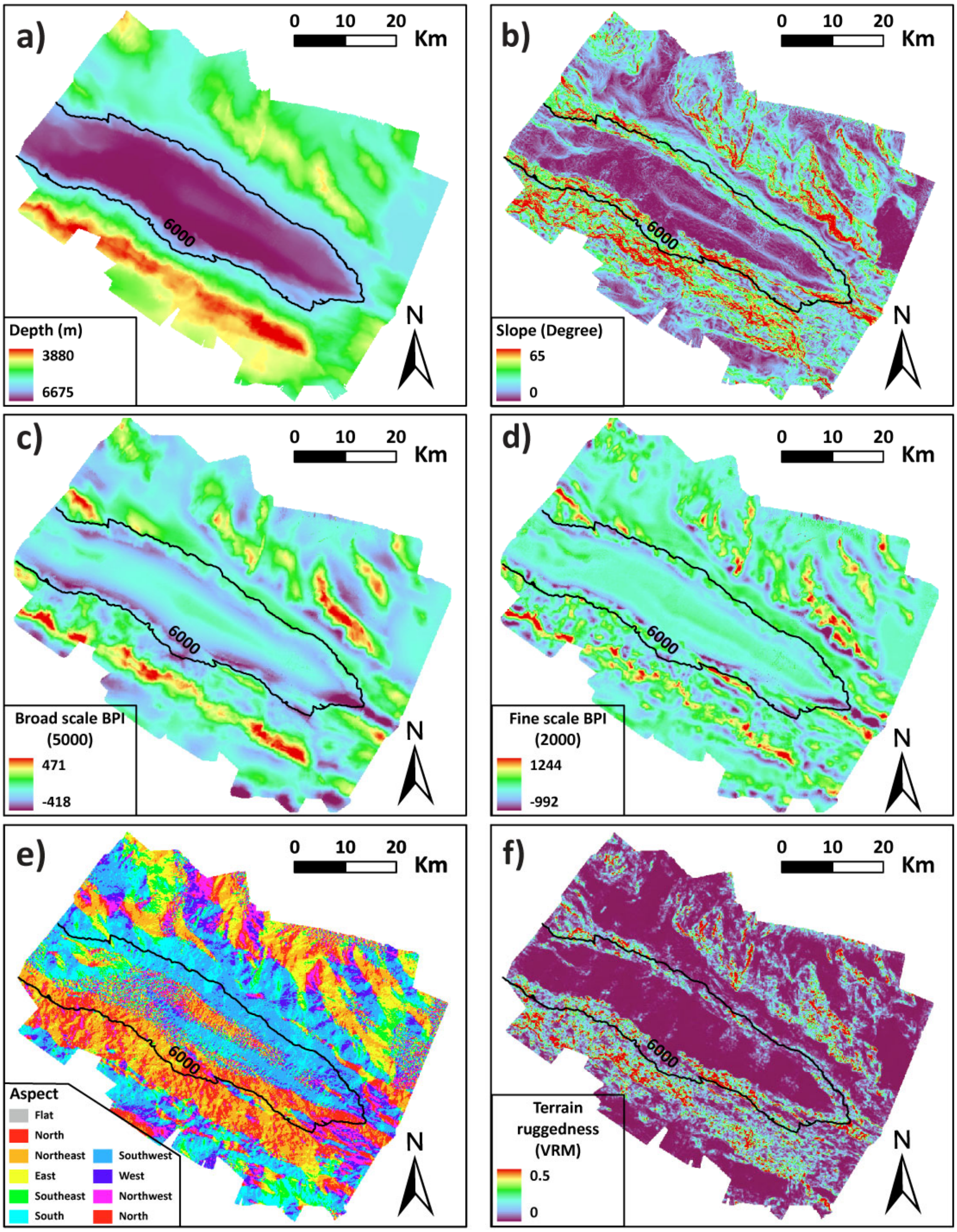

Figure 5. Multibeam bathymetry and derivatives used in this study. (a) Bathymetry, (b) Slope, (c) Broad scale BPI (Bathymetric Position Index), (d) Fine scale BPI, (e) Aspect and (f) Terrain Ruggedness Index. 6000 m contour line is labelled in all figures.

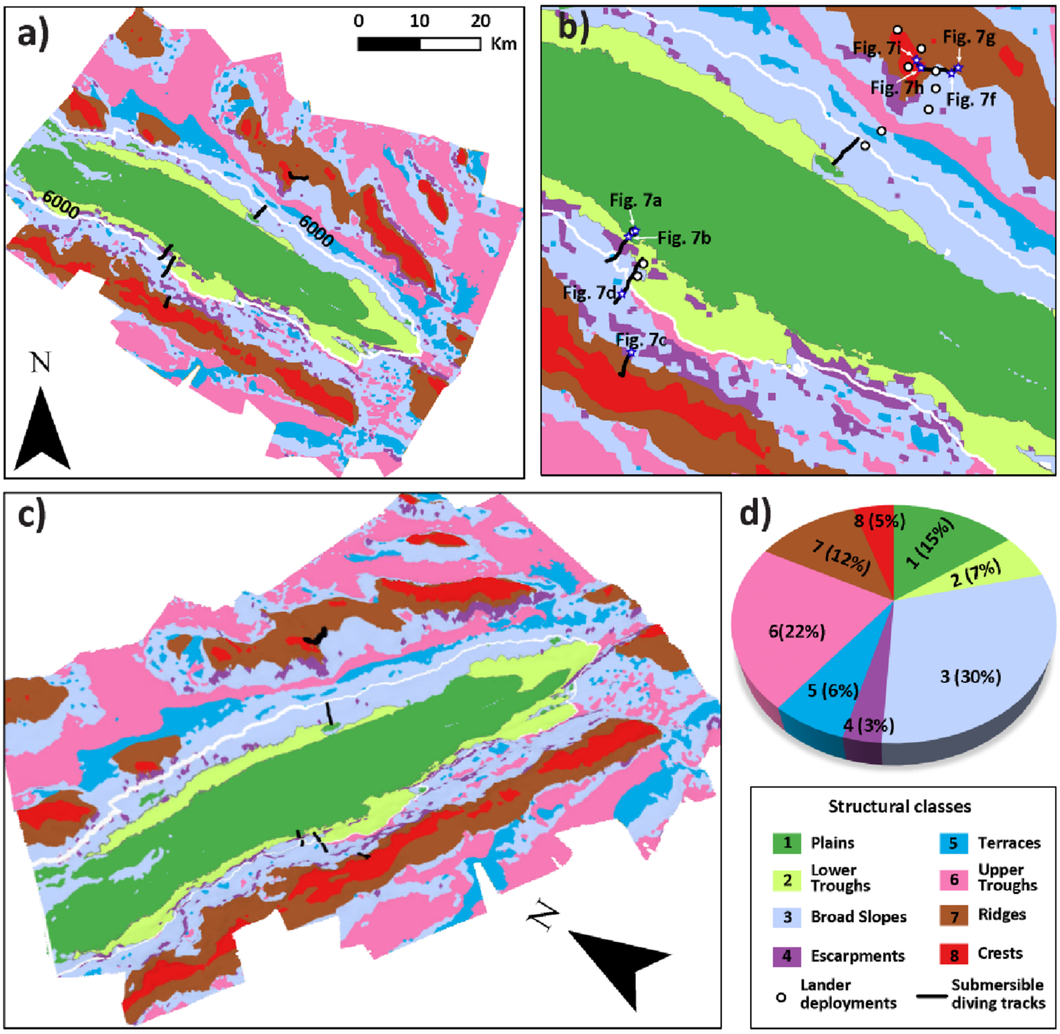

Figure 6. Structural classed identified using Benthic Terrain Modeler. (a) Plan-view map of the structural classes. (b) Zoom in map of the lander sites and submersible diving tracks with the structural classes. Stars represent location of images shown in Figure 7. (c) Oblique 3D visualization of the structural classes. (d) Pie chart showing the proportion of each class.

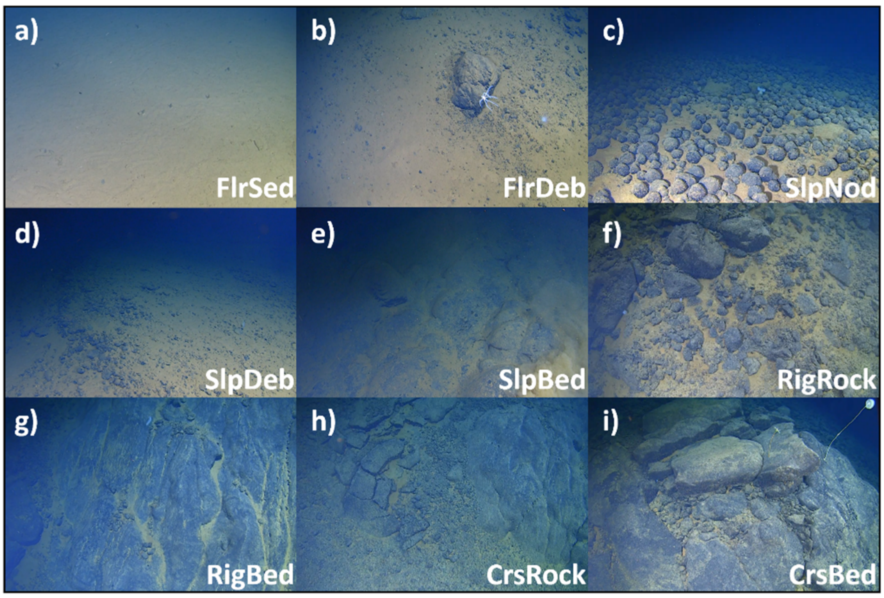

Figure 7. Habitat units observed during the submersible dives. (a) Plain Floor Sediments (FlrSed), (b) Plain Floor Debris (FlrSed), (c) Slope Nodules (SlpNod), (d) Slope debris (SlpDeb), (e) Slope Bedrocks (SlpSed), (f) Rocky Ridge Walls (RigRock),, (g) Ridge Bedrocks (RigBed),, (h) Crests covered by rocks and granular (CrsRock), and (i) Cres Bedrocks (CrsBed). Location of these images were marked in Figure 6b.

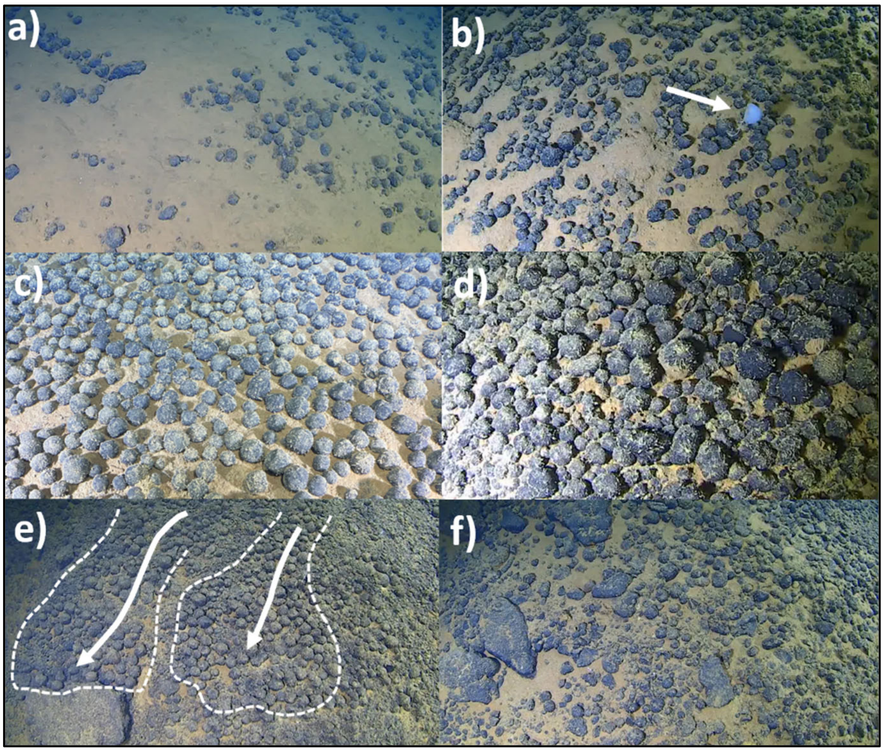

Figure 8. Nodules from different locations with different characteristics. (a) – (d) represent polymetallic nodules that show increasing trend of densities and coverage. Note the fauna highlighted by white arrow in (b) is attached to the nodules. (e) shows lobate shaped accumulation of nodules due to downslope transportation. (f) Soft sediments are increased, nodules become rare and started to merge with crust.

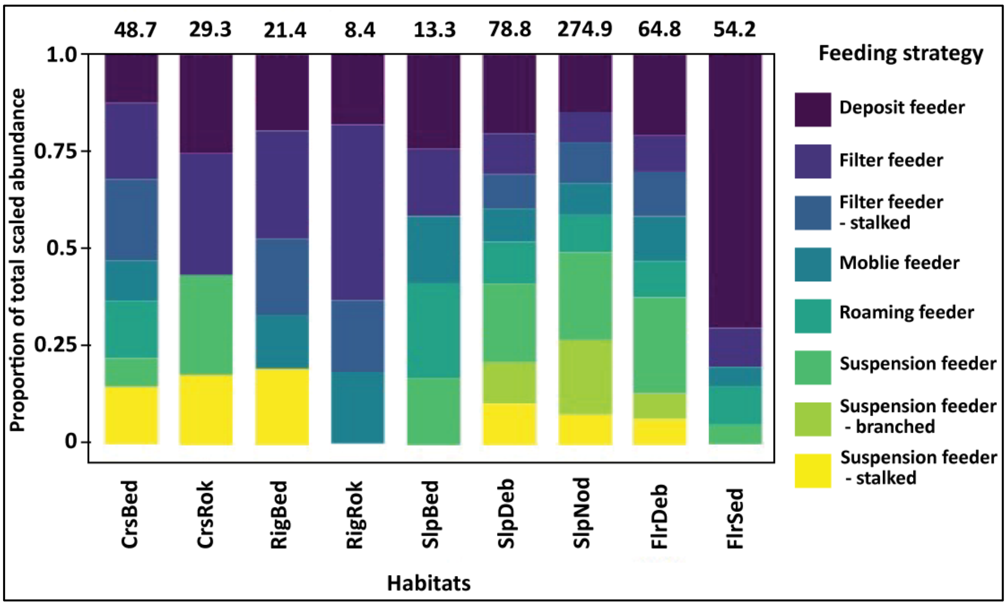

Figure 9. Functional feeding groups identified in submersible video footages and their distribution in each habitat unit in the Wallaby-Zenith Fracture Zone.

Tables

Table 1. Deployment details of landers in the Wallaby-Zenith Fracture Zone. Latitudes and longitudes are in decimal degree.

Deployments	Date	Station ID	Latitude (East)	Longitude (South)	Depth (m)
1	May 14, 2021	WZFZ_CL1	22.201	102.5222	6409
2	May 14, 2021	WZFZ_SK1	22.2118	102.522	5162
3	May 14, 2021	WZFZ_FL1	22.201	102.5222	4967
4	May 15, 2021	WZFZ_FL2	22.2248	102.517	5450
5	May 15, 2021	WZFZ_SK2	22.2378	102.4852	5734
6	May 15, 2021	WZFZ_CL2	22.2468	102.474	5931
7	May 17, 2021	WZFZ_CL3	22.1749	102.497	4709
8	May 17, 2021	WZFZ_SK3	22.1868	102.5128	4648
9	May 17, 2021	WZFZ_FL3	22.198	102.5038	4691
10	May 18, 2021	WZFZ_FL4	22.2978	102.3178	6591
11	May 18, 2021	WZFZ_SK4	22.318	102.324	6326
10	May 18, 2021	WZFZ_CL4	22.3257	102.32	6187

Table 2. Deployment details of submersible diving in the Wallaby-Zenith Fracture Zone. Latitudes and longitudes are in decimal degree. Start and end depths represent the depth when the submersible arrives at and leaves from the sea bottom.

Deployments	Date	Diving ID	Start			End			Total surveying time (minute)
			Latitude (East)	Longitude (South)	Depth (m)	Latitude (East)	Longitude (South)	Depth (m)	
1	May 15, 2021	WZFZ_LF1	- 22.2575	102.4528	6384	22.2423	102.4694	6040	212
2	May 17, 2021	WZFZ_LF2	22.2005	102.5225	4950	22.1924	102.5094	4570	264
3	May 18, 2021	WZFZ_LF3	22.2975	102.3188	6575	22.3163	102.2993	5900	263
4	May 20, 2021	WZFZ_LF4	22.3148	102.3233	6325	22.3418	102.3043	5580	149
5	May 21, 2021	WZFZ_LF5	22.3732	102.3147	5215	22.3862	102.3068	4475	202
6	May 22, 2021	WZFZ_LF6	22.2000	102.5213	4969	22.1997	102.5364	4915	180

Table 3. Decision table summarizing the thresholds used for the definition of seafloor structural classes in the Wallaby-Zenith Fracture Zone.

Class ID	Structural classes	Broad BPI		Fine BPI		Slope (degree)		Depth (m)	
		Lower	Upper	Lower	Upper	Lower	Upper	Lower	Upper
1	Plains	-100	100	-150	300		6		6000
2	Lower Troughs								6000
3	Broad Slopes	-100	100		300	6	18		
4	Escarpments		100	-150	300	18			
5	Terraces	-100	100	-150	300		6	6000	
6	Upper Troughs		100		0			6000	
7	Ridges	100		300					
8	Crests	100		-150	300				

Table 4. Areal coverage and depth-related zonal statistics of each structural classes.

Class ID	Structural class	Area (km^2)	Percentage (%)	Maximum depth (m)	Minimum depth (m)	Median (m)	Mean depth (m)	Standard deviation
1	Plains	568	14.8	6707	6103	6578	6558	72
2	Lower Troughs	243	6.3	6638	5949	6450	6402	163
3	Broad Slopes	1140	29.8	6620	4315	5468	5492	467
4	Escarpments	123	3.2	6593	4389	5543	5611	427
5	Terraces	241	6.3	6000	4356	5478	5316	439
6	Upper Troughs	854	22.3	6049	4390	5517	5398	373
7	Ridges	470	12.3	5767	4030	4777	4777	342
8	Crests	188	4.9	5658	3880	4469	4534	382

Table 5. Seafloor habitat units differentiated along submersible dive tracks and associated seafloor structures (Complied from Greene et al., 1999 and 2007).

Habitat ID	Habitat units	Structural class (Mesohabitats)	Subclass	Modifiers	Dives
1	Floor Sediments (FlrSed)	Plains and Lower Troughs	Slope <6°; Mixed mud and ooze; Mean temperature: 1.24 ˚C; Mean salinity: 34.72 psu. Water mass: AABW	Patchy bioturbation tracks; Little cover of xenophyophores.	WZFZ-LF2 and 3
2	Floor Debris (FlrDeb)	Plains and Lower Troughs	Slope <6°; Mud overlain by mixed gravels to boulders; Mean temperature: 1.24 ˚C; Mean salinity: 34.72 psu. Water mass: AABW	Poorly sorted, angular, and unconsolidated black gravels; Occasional to contiguous coverage.	WZFZ-LF3 and 4
3	Slope Nodules (SlpNod)	Terraces and Slopes	Slopes >6°; Mud and ooze coated by nodules; Mean temperature: 1.22 ˚C; Mean salinity: 34.72 psu. Water mass: AABW	Little cover to continuous nodules; Nodules were dusted.	WZFZ-LF2 to 5
4	Granular Debris (SlpDeb)	Slopes	Mixed mud and granular rock fragments above black basement rocks; Mean temperature: 1.22 ˚C; Mean salinity: 34.72 psu. Water mass: AABW	Poorly sorted, mostly round-shaped gravels. Dusted.	WZFZ-LF4 and 6
5	Slope Bedrock (SlpBed)	Slopes	Smooth rock faces, likely a pillow lava field; Mean temperature: 1.22 ˚C; Mean salinity: 34.72 psu. Water mass: AABW	Little gravles and thin sediments coverage.	WZFZ-LF3, 4 and 6
6	Rocky Ridge Walls (RigRock)	Ridges	Mixed sediments; Mean temperature: 1.22 ˚C; Mean salinity: 34.72 psu. Water mass: AABW	Stratified boulders; Sediment pockets,	WZFZ-LF2
7	Ridge Wall Bedrocks (RigBed)	Ridges	Smooth bedrock surface; Mean temperature: 1.22 ˚C; Mean salinity: 34.72 psu. Water mass: AABW	Bedrocks with thin sediment covearage.	WZFZ-LF2
8	Rocky Crests (CrsRock)	Crests	Rock fractures along the joints; Mean temperature: 1.35 ˚C; Mean salinity: 34.71 psu. Water mass: AABW	Poorly sorted, mixed cobbles to boulders, occasional sediment pockets.	WZFZ-LF2
9	Crest Bedrock (CrsBed)	Crests	Smooth bedrock surface; Mean temperature: 1.35 ˚C; Mean salinity: 34.71 psu.	Occasional gravels, thin sediments.	WZFZ-LF2

			Water mass: AABW		

Table 6. Abundance of organisms recorded in each habitat unit and the total time spent surveying each unit by crewed submersible dives.

Habitat ID	Habitat units	Total abundance	Survey time (mins)	Number of ind. min-1
1	Floor Sediments (FlrSed)	211	54.2	3.90
2	Floor Debris (FlrDeb)	36	64.8	0.56
3	Slope Nodules (SlpNod)	149	274.9	0.54
4	Granular Debris (SlpDeb)	38	78.8	0.48
5	Slope Bedrock (SlpBed)	7	13.3	0.53
6	Rocky Ridge Walls (RigRock)	9	8.4	1.07
7	Ridge Wall Bedrocks (RigBed)	11	21.4	0.51
8	Rocky Crests (CrsRock)	8	29.3	0.27
9	Crest Bedrock (CrsBed)	29	48.7	0.60